

# Regulating Electronic Conductivity at Cathode Interface for Low-Temperature Halide-Based All-Solid-State Batteries

Sixu Deng, Ming Jiang, Ning Chen, Weihan Li, Matthew Zheng, Weifeng Chen, Ruying Li, Huan Huang, Jiantao Wang,\* Chandra Veer Singh,\* and Xueliang Sun\*

Halide solid-state batteries (SSBs) show unparalleled application potential because of their outstanding advantages, such as high ionic conductivity and good compatibility with cathodes. However, operating halide SSBs under freezing temperatures faces big challenges, and the underlying degradation mechanisms are unclear. Herein, the impact of electronic conductivity in low-temperature halide SSBs is investigated by designing different additives in the composite cathode. It is shown that the electrochemical stability of a halide electrolyte ( $\text{Li}_3\text{InCl}_6$ ) with additives is significantly affected by the degree of electronic conductivity as well as the ambient operational temperature. When the ambient temperatures are below freezing point, the moderate electronic conductivity in the composite cathode is beneficial toward improving the charge transfer kinetics without inducing the decomposition of  $\text{Li}_3\text{InCl}_6$ . The electrode materials ( $\text{LiCoO}_2$  cathode and  $\text{Li}_3\text{InCl}_6$  electrolytes) show excellent structural and interfacial stability during electrochemical reactions, resulting in a competitive performance at low temperatures. Stable long-term cycling performance with a capacity retention of 89.2% after 300 cycles is achieved along with a C-rate capacity of 77.6 mAh  $\text{g}^{-1}$  (0.6 C) at  $-10^\circ\text{C}$ . This in-depth study investigates the role of electronic conductivity, which opens the door to future research on low-temperature SSBs.

safety issues of traditional lithium-ion batteries in electric vehicles (EVs).<sup>[1]</sup> Furthermore, high energy densities of over 500 Wh  $\text{kg}^{-1}$  are expected to be achieved after successfully applying the high-capacity anodes.<sup>[2]</sup> As the critical component in solid-state batteries (SSBs), the performances of SSEs determine the entire performance of SSBs. Halide-based SSEs, as a rising star in inorganic SSBs, are considered as one of the most promising SSEs that can be applied in EVs because of their excellent properties. Compared to sulfide-based inorganic SSEs, halide-based SSEs have a higher electrochemical stability window, therefore having better compatibility with most lithium-ion cathodes including the high-capacity Ni-rich cathodes.<sup>[3]</sup> In addition, the enhanced air stability and the developed solution-based synthesis methods greatly improve the possibility of industrial scale-up for halide-based SSBs.<sup>[4]</sup> However, the application of halide-based SSBs is still limited by some key challenges. On the one hand, there is poor

interfacial stability between halide SSEs and Li anodes, which is a big concern for realizing the target of high energy density.<sup>[5]</sup> On the other hand, the ionic conductivity of halide SSEs still falls behind that of sulfide SSEs. As a result, the rate capability of halide-based SSBs at high current densities has room for improvement.

## 1. Introduction

Solid-state lithium-ion batteries (SSLIBs) have developed rapidly in the past five years because of their outstanding advantages. In particular, using nonflammable solid-state electrolytes (SSEs) to replace organic liquid electrolytes avoids the related

S. Deng, W. Li, M. Zheng, R. Li, X. Sun  
Department of Mechanical and Materials Engineering  
University of Western Ontario  
London, Ontario N6A 5B9, Canada  
E-mail: xsun9@uwo.ca

M. Jiang  
Institute of Physical Science and Information Technology  
Anhui University  
Hefei 230601, P.R. China

N. Chen, W. Chen  
Canadian Light Source  
44 Innovation Boulevard, Saskatoon, Saskatchewan S7N 2V3, Canada

H. Huang  
Glabat Solid-State Battery Inc.  
London, Ontario N6G 4x8, Canada

J. Wang  
China Automotive Battery Research Institute Co. Ltd  
Beijing 100088, P.R. China  
E-mail: wangjt@glabat.com

M. Jiang, C. V. Singh  
Department of Materials Science and Engineering  
University of Toronto  
Toronto, Ontario M5S 3E4, Canada  
E-mail: chandraveer.singh@utoronto.ca

 The ORCID identification number(s) for the author(s) of this article can be found under <https://doi.org/10.1002/adfm.202205594>.

DOI: 10.1002/adfm.202205594

In addition, EVs require SSBs capable of delivering stable performance under extreme conditions such as operating in a cold climate.<sup>[6]</sup> Unfortunately, SSBs face tremendous challenges when operating at low temperatures. For example, the ionic conductivity of SSEs dramatically drops with a decrease in temperature, resulting in slow kinetics of Li<sup>+</sup> transport both in the SSEs and at the solid-solid interfaces.<sup>[7]</sup> So far, increasing the ionic conductivity of SSEs is a common strategy to improve SSBs performance at low temperatures. In polymer-based SSBs, decreasing the crystallization is a common method to increase the ionic conductivity of SSEs and has been proved effective in improving the electrochemical performance at low temperatures.<sup>[8]</sup> The efforts on low-temperature sulfide-based SSBs have been made by manipulating the ionic conductivity of sulfide SSEs and stabilizing their interfaces. For example, Yu et al. developed a series of chlorine-rich argyrodite SSEs with high ionic conductivities and applied the coating to stabilize the cathode interface. As a result, the sulfide SSBs exhibited improved electrochemical performance under freezing temperatures.<sup>[9]</sup> In addition, developing new SSEs is considered a promising solution to address the challenges of SSBs at low temperatures. For example, nano-sized metal-organic frameworks (MOFs) SSE was developed with a high Li<sup>+</sup> transference number and an effective suppression of lithium dendrite growth.<sup>[10]</sup> The SSB, assembled with LiFePO<sub>4</sub> as the cathode, showed a stable cycling performance at 0 °C.

Compared to other SSEs, the research on low-temperature halide SSBs is absent and the degradation mechanisms are not well understood. In addition to reduced ionic conductivity at low temperatures, whether and how the electronic conductivity in the cathode layer affects the performance of SSBs is not clear and worthy of being studied. In sulfide-based SSBs, the application of conductive additives is a challenge. Because of sufficient electronic percolation pathways provided by conductive additives, the decomposition of sulfide SSEs is severe at room temperature.<sup>[11]</sup> As a result, the formed undesirable interface deteriorates the performance of SSBs. Even at low temperatures, the application of carbon in cathode layer also leads to the decomposition of sulfide SSEs, resulting in decayed cycling stability.<sup>[12]</sup> Hence, investigating the effect of electronic conductivity in halide-based SSBs, particularly at low temperatures, is critical toward high-performance SSBs under a wide temperature range.

In this paper, the electronic conductivity in the cathode layer of halide SSBs is manipulated by designing additives with different electronic conductivities. Carbon nanotubes (CNTs) are added to the cathode layer as the conductive additive while adding poly(3,4-ethylenedioxythiophene) (PEDOT) in cathode layer exhibits a semi-conductive property. When mixing only the halide SSE (Li<sub>3</sub>InCl<sub>6</sub>, denoted as LIC) and cathode material (LiCoO<sub>2</sub>, denoted as LCO) to form the cathode layer, the entire cathode demonstrates an electronically isolated property. The density functional theory (DFT) calculations combined with electrochemical analyses and X-ray photoelectron spectroscopy (XPS) characterization indicate that the high electronic conductivity of additives does not induce the decomposition of LIC at low temperatures. Instead, high electronic conductivity significantly improves charge transfer kinetics, which is critical for electrochemical performance at low temperatures. LIC SSB

with CNTs as an additive shows the best C-rate capability at -10 °C with a capacity of 77.6 mA h g<sup>-1</sup> at 0.6 C and exhibits impressing long-term cycling stability with a capacity retention of 89.2% after 300 cycles. The X-ray absorption spectroscopy (XAS) and XPS results reveal that SSBs with high electronic conductivities possess excellent structural and interfacial stability after cycling at -10 °C. The scientific insights gained on the impact of electronic conductivity in low-temperature SSBs provide an important guideline for the future design of high-performance all-climate SSBs.

## 2. Results and Discussion

The electronic properties of LIC, PEDOT, and CNTs are calculated by DFT. Their atomic structures are shown in Figure S1 (Supporting Information). The density of state (DOS) of LIC, PEDOT, and CNTs is calculated based on their relaxed structures, as shown in Figure 1a–c. LIC shows an obvious band gap of 3.1 eV, indicating its insulating character. In contrast, the band gap of PEDOT is computed as 0.8 eV, suggesting that PEDOT is a semi-conductive material. Because of the absence of an energy gap, CNTs exhibit a metallic character. Based on these observations, it is proposed that CNTs would have good electronic conductivity when applied in the composite cathode as an additive. The electronic conductivity of LIC, PEDOT, and CNTs is also calculated at 25 °C and -10 °C, respectively (Figure 1d). The carrier (electron) relaxation time is set to be  $\approx 10^{-14}$  s as per the Materials Project.<sup>[13]</sup> The carrier concentration is set at the range of  $10^{15}$ – $10^{17}$  cm<sup>-3</sup>. At 25 °C, the electronic conductivity of three materials is CNTs > PEDOT > LIC, which is consistent with the DOS results. Interestingly, at -10 °C, the electronic conductivity of CNTs maintains at the same level as at 25 °C. In contrast, the electronic conductivity of PEDOT at -10 °C drops to a level similar to LIC at 25 °C. Meanwhile, LIC also shows a decreased electronic conductivity at -10 °C. In addition to electronic conductivity, the electron transfer between LIC, CNTs, and cathode materials (LCO) is evaluated by the calculation of electrostatic potentials. As shown in Figure 1e,f, the electrostatic potential of LCO/LIC interface is 2.98 eV, which is 3.5 times higher than that of the LCO/CNTs interface. This result suggests that the electron transfer at LCO/CNTs interface is much easier than at the LCO/LIC interface. The DFT results suggest that CNTs exhibit higher electronic conductivity at both 25 °C and -10 °C than PEDOT and LIC, and show a more favorable electron interface with the LCO cathode.

In SSBs, the high ionic conductivity of SSEs is crucial for good electrochemical performance. The Arrhenius plot of LIC SSE derived from electrochemical impedance spectroscopy (EIS) measurements is shown in Figure 2a. The ionic conductivity of LIC SSE is only  $1.6 \times 10^{-4}$  S cm<sup>-1</sup> at -10 °C, which is six times lower than that of 25 °C. The electronic conductivity of LIC SSE is measured by a chronoamperometry (CA) method in the symmetric cell (Figure S2, Supporting Information). As shown in Figure 2b, the electronic conductivity of LIC is only  $2.1 \times 10^{-9}$  S cm<sup>-1</sup> at 25 °C and drops down to  $4.3 \times 10^{-10}$  S cm<sup>-1</sup> at -10 °C. Although the ultralow electronic conductivity of SSE is beneficial toward avoiding self-discharge and stabilizing Li anode, the electron transfer in cathode layer is highly limited.

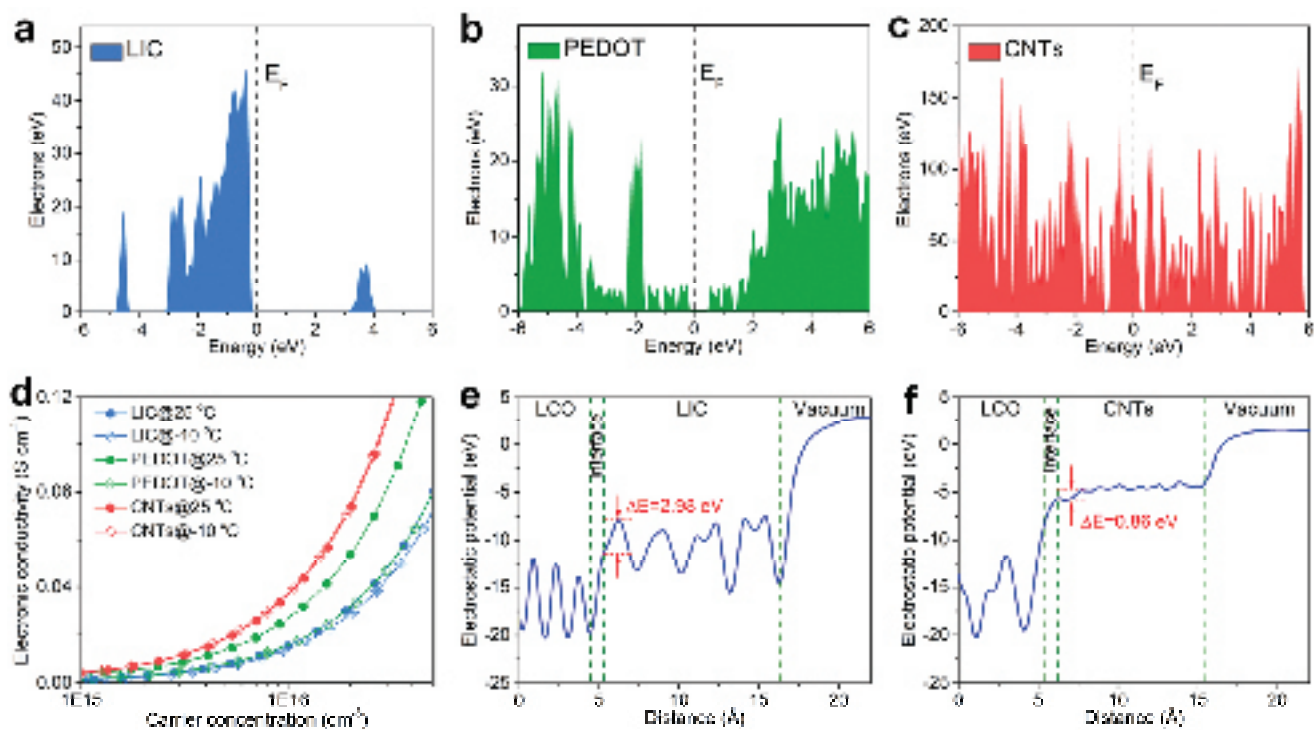


**Figure 1.** Electronic properties of LIC, PEDOT, and CNTs calculated by DFT calculations. Total density of states of a) LIC, b) PEDOT, and c) CNTs (the Fermi level is set to be 0 eV), d) electronic conductivity of LIC, PEDOT, and CNTs at 25 °C and -10 °C, the electrostatic potential profiles for e) LCO/LIC and f) LCO/CNTs.

After adding CNTs as additives, the electronic conductivity improves to  $3.3 \times 10^{-9} \text{ S cm}^{-1}$  at 25 °C. Compared to LIC, LIC/PEDOT and LIC/CNTs exhibit an electronic conductivity of  $2.6 \times 10^{-9}$  and  $3.3 \times 10^{-9} \text{ S cm}^{-1}$ , respectively. However, the electronic conductivity of LIC/PEDOT decreases to  $4.3 \times 10^{-10} \text{ S cm}^{-1}$  at -10 °C. Although the electronic conductivity of LIC/CNTs also decreased, it can still maintain at  $1.1 \times 10^{-9} \text{ S cm}^{-1}$ .

To investigate the electrochemical stability of LIC SSE after combining with additives, three different model cells are designed as shown in Figure 2c. Double-layer SSE design is adopted, in which a sulfide  $\text{Li}_6\text{PS}_5\text{Cl}$  (LPSCl) SSE faces the In-Li anode and LIC SSE contacts with the cathode layer. In the cathode layer, LIC, PEDOT mixed with LIC, and CNTs mixed with LIC are employed for the following electrochemical testing and characterizations. The mass ratio between LIC and additives (PEDOT or CNTs) in the mixed cathode layer is 7:3, which is the same as the commonly used ratio in other reported works.<sup>[14]</sup> The chemical stability of LIC with additives is first studied by X-ray powder diffraction (XRD) (Figure S3, Supporting Information). After 24 h rest, there is no observed structure evolution of LIC after mixing with PEDOT or CNTs. Because of the same morphology and amount of PEDOT and CNTs, the electrochemical stability of LIC SSE is only affected by the degree of electronic conductivity of additives. To better understand the electrochemical behaviors at -10 °C, the above three model cells are first tested at 25 °C. Cyclic voltammogram (CV) profiles of three model cells at 25 °C are shown in Figure S4 (Supporting Information). An obvious anodic peak is observed at 3.02 V (vs  $\text{Li}^+/\text{Li-In}$ ) in the LIC/CNTs cell during the first CV cycle. At the second CV cycle, this anodic peak

moves to 3.41 eV along with the increased current from 0.51 to 0.55  $\text{mA g}^{-1}$ , suggesting the continued decomposition of LIC. Compared to the LIC/CNTs cell, there is no obvious anodic peak in the LIC/PEDOT cell, suggesting a suppression in the decomposition of LIC because of the lower electronic conductivity of PEDOT. The EIS plots of three cells before and after CV testing at 25 °C are shown in Figure S3c–e (Supporting Information). The increased resistance in the LIC/CNTs cell can be attributed to the decomposition of LIC. Compared to our previous study in sulfide-based SSEs,<sup>[15]</sup> the electrochemical stability between LIC and additives is much better, but not entirely stable at 25 °C. When CV testing is conducted at -10 °C, no obvious anodic peak is observed in the LIC/CNTs cell during the first CV cycle, as shown in Figure 2d. In addition, the polarization current of LIC/CNTs cell at 3.6 V is also much lower than that of the LIC/CNTs cell at 25 °C. Moreover, the intensities of the current significantly decrease at the second CV cycle, suggesting a more stable interface is formed at -10 °C compared to 25 °C. To further evaluate the electrochemical stability between LIC SSE and additives at -10 °C, X-ray photoelectron spectroscopy (XPS) characterization is conducted for the CV cycled cathode pellets, as shown in Figure 2e,f and Figure S5 (Supporting Information). Both In 3d and Cl 2p XPS spectra reveal no distinctive peak and no obvious change of peak position after CV testing. This result indicates good electrochemical stability between LIC SSE and additives at -10 °C, which can be corroborated by the EIS results as shown in Figure S6 (Supporting Information).

In addition, the effect of ambient temperatures on the electrochemical stability between LIC SSE and additives is also

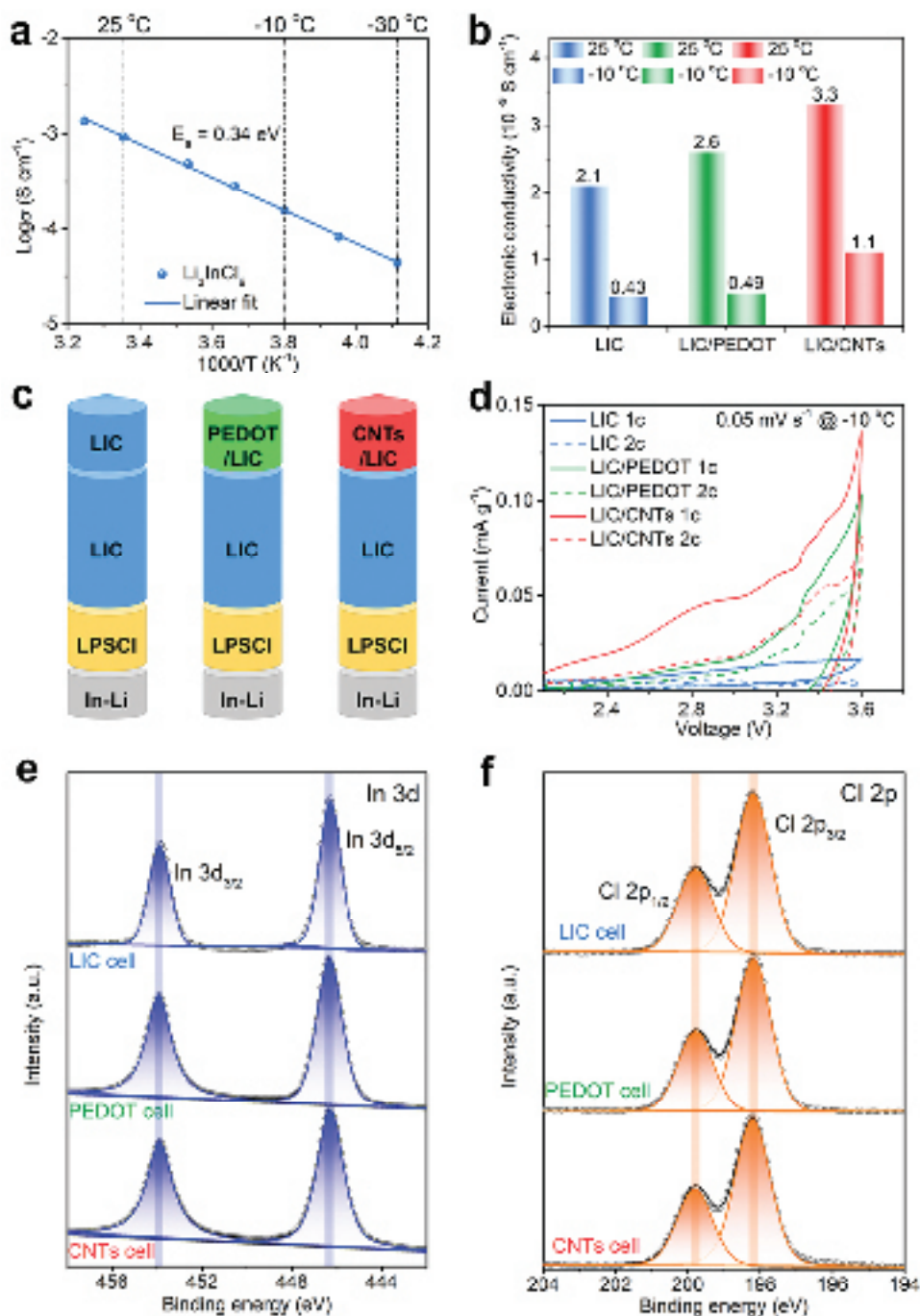


**Figure 2.** Investigating the electrochemical stability of LIC SSE combined with different additives at  $-10 \text{ }^\circ\text{C}$ . a) Arrhenius plots of LIC SSEs derived from the EIS measurements in a range of  $-30 \text{ }^\circ\text{C}$  to  $35 \text{ }^\circ\text{C}$ , b) electronic conductivity of LIC, LIC/PEDOT composite, and LIC/CNTs composite at  $25 \text{ }^\circ\text{C}$  and  $-10 \text{ }^\circ\text{C}$ , c) schematic illustration of the designed model cells for CV test; d) CV profiles at  $-10 \text{ }^\circ\text{C}$ , e) In 3d and f) Cl 2p XPS spectra of LIC cell, LIC/PEDOT cell, and LIC/CNTs cell after CV test.

investigated in this study. CV tests are conducted at  $25 \text{ }^\circ\text{C}$ ,  $-10 \text{ }^\circ\text{C}$ , and  $-30 \text{ }^\circ\text{C}$ , respectively. The LIC/CNTs cell is selected for demonstration because of the high electronic conductivity of CNTs (Figure 3a). From the CV profiles of the first cycle shown in Figure 3b, an obvious onset potential can be observed at  $2.66 \text{ V}$  in the  $25 \text{ }^\circ\text{C}$  cell, which is much lower than the onset potentials of  $3.11 \text{ V}$  in the  $-10 \text{ }^\circ\text{C}$  cell and  $3.19 \text{ V}$  in the  $-30 \text{ }^\circ\text{C}$

cell. Meanwhile, a high polarization current of  $0.28 \text{ mA g}^{-1}$  can be detected in the  $25 \text{ }^\circ\text{C}$  cell. In contrast, the polarization currents in the  $-10 \text{ }^\circ\text{C}$  cell and  $-30 \text{ }^\circ\text{C}$  cell are only  $0.14$  and  $0.06 \text{ mA g}^{-1}$ , respectively. During the second CV cycle, the polarization current in the  $25 \text{ }^\circ\text{C}$  cell continues increasing to  $0.71 \text{ mA g}^{-1}$  (Figure 3c), suggesting a continuous decomposition of LIC at  $25 \text{ }^\circ\text{C}$  catalyzed by CNTs. Impressively, the

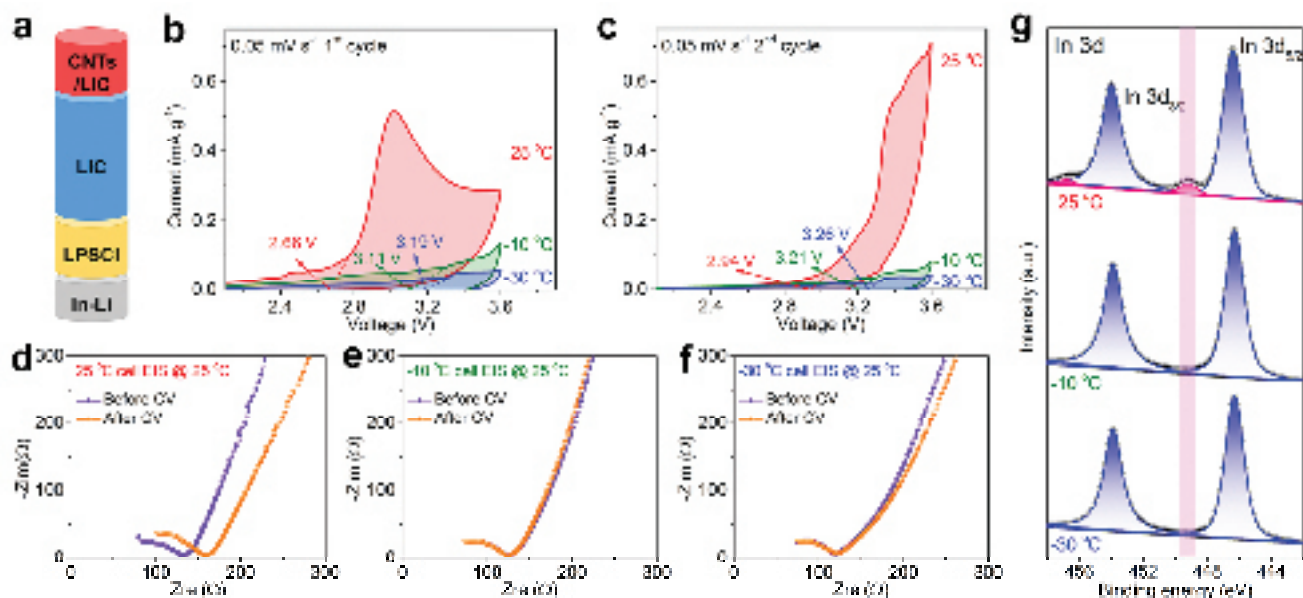


**Figure 3.** Investigating the electrochemical stability of LIC/CNTs cell at different temperatures. a) Schematic illustration of the designed model cell; CV profiles at the b) first and c) second cycles; EIS spectra before and after CV cycles of d) 25 °C cell, e) –10 °C cell, and f) –30 °C cell; g) In 3d XPS spectra after CV test.

polarization currents in both –10 °C cell and –30 °C cell are decreased with the higher onset potentials compared to the first CV cycle. This result suggests that the interface between LIC SSE and CNTs tends to be stable during the CV process at low temperatures. The EIS spectra before and after CV cycles are shown in Figure 3d–f. For comparison under the same condition, all EIS testing is conducted at 25 °C. After the CV testing, only 25 °C cell shows an increased resistance, suggesting the formation of an undesired interface between LIC SSE and CNTs. From In 3d and Cl 2p XPS spectra as shown in Figure 3g and Figure S7 (Supporting Information), the by-products can be detected in the 25 °C cell. In contrast, the interface between LIC SSE and CNTs is stable at low temperatures, which is consistent with the CV and EIS results. It should be noticed that when the mass ratio between LIC and CNTs in cathode layer decreases to 30:1, the decomposition of LIC can be significantly suppressed as shown in Figures S8 and S9 (Supporting Information). The above results indicate that ambient temperature is critical for the electrochemical stability of LIC SSE after being combined with conductive additives. In addition, the amounts of CNTs in cathode layer are also very important to affect the degree of degradation of LIC.

The electrochemical performance at –10 °C is evaluated in the LCO-based SSBs. CNTs and PEDOT are respectively adopted as additives and are mixed with bare LCO and LIC to form the cathode layer. Three types of cathode layers are demonstrated in this study for comparison, including LCO mixed with LIC, LCO mixed with LIC together with PEDOT, and LCO mixed with LIC together with CNTs. They are denoted as LIC cell, PEDOT cell, and CNTs cell, respectively. The detailed electrode process for the fabrication of SSBs is described in the experimental section. The scanning electron microscope (SEM) images and energy dispersive spectrometer (EDS) mappings of the prepared composite cathodes are shown in

Figures S10–S12 (Supporting Information). Both PEDOT and CNTs are contacted with LCO and LIC, which is beneficial for electron transfer at the cathode/SSE/additive three-phase interface. The electrochemical performance is first tested at 25 °C. At a current density of 0.05 C, all three cells show similar initial discharge capacities of 131.1 mA h g<sup>–1</sup> (LIC cell), 132.9 mA h g<sup>–1</sup> (PEDOT cell), and 133.6 mA h g<sup>–1</sup> (CNTs cell), respectively (Figure S13, Supporting Information). In contrast, the initial discharge capacity of LIC cell is only 103.1 mA h g<sup>–1</sup> at –10 °C, as shown in Figure 4a and Figure S14 (Supporting Information). With increasing electronic conductivity of additives, the discharge capacity increases from 119.5 mA h g<sup>–1</sup> in the PEDOT cell to 127.0 mA h g<sup>–1</sup> in the CNTs cell, as shown in Figure 4b,c. Notably, the more obvious voltage plateaus derived from the phase transition of LCO can be observed in the CNTs cell at both the end of charge and the beginning of discharge. This phenomenon suggests faster Li<sup>+</sup> and electron transfer in the CNTs cell, which is benefiting from the high electronic conductivity of CNTs. Furthermore, CNTs cell shows the highest Coulombic efficiency and average discharge voltage with the lowest irreversible capacity loss at the first charge-discharge cycle, as shown in Figure 4d. The corresponding differential capacity profiles as a function of voltage are shown in Figure 4e, which further reveal the different charge-discharge behaviors before and after adding the additives. CNTs cell demonstrates the smallest voltage intervals between the pairs of anodic-cathodic peaks and the highest peak intensities, suggesting an enhanced electrochemical reaction activity with lower resistance in the cathode layer.

To gain further insight into the charge transfer kinetics in the cathode layer, the galvanostatic intermittent titration technique (GITT) testing is conducted at –10 °C, and the charge-discharge curves are shown in Figure S15 (Supporting Information). The lithium-ion diffusion coefficients ( $D_{Li}$ ) during

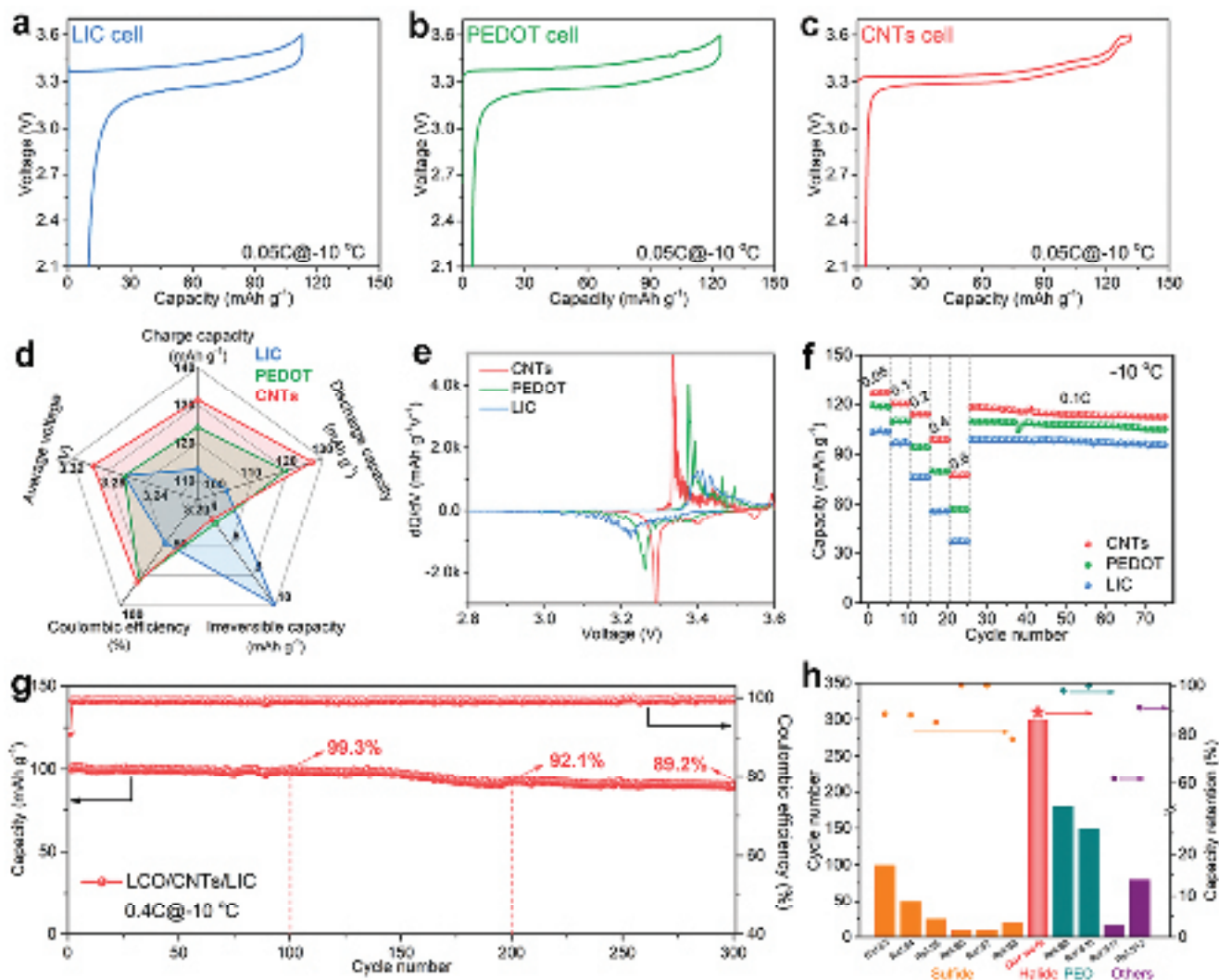


**Figure 4.** Effect of additives on the electrochemical performance of SSBs at  $-10\text{ }^{\circ}\text{C}$ . a–c) Charge–discharge curves of the first cycle at  $0.05\text{ C}$ ; the corresponding d) performance parameters and e) differential capacity profiles collected from charge–discharge curves; f) rate and cycling stability; g) long-term cycling stability of ASSLIB with CNTs as an additive, and h) comparison of low-temperature performance between this work and other SSBs from literature.

the charge and discharge processes are calculated and shown in Figure S16 (Supporting Information). CNTs cell exhibits the highest  $D_{\text{Li}}$  with the smallest polarization potential during the entire charge–discharge cycle. This result indicates that the charge transfer kinetics can be enhanced by adding a high electronically conductive additive in the cathode layer. The C-rate and cycling performances of the three cells are shown in Figure 4f and Figure S17 (Supporting Information). At  $25\text{ }^{\circ}\text{C}$ , the rate capacities of the three cells are similar at  $0.05\text{ C}$ ,  $0.1\text{ C}$ , and  $0.2\text{ C}$ , indicating electronic conductivity is not the limitation for LCO/LIC SSBs at low current densities because of the high ionic conductivity ( $1.4 \times 10^{-3}\text{ S cm}^{-1}$ ) of LIC at room temperature. When the current densities reached  $0.4\text{ C}$  and  $0.6\text{ C}$ , the high electronic conductivity from CNTs contributes to charge transfer kinetics in the cathode layer, resulting in higher capacities. Compared to the performance at  $25\text{ }^{\circ}\text{C}$ , the rate capability at  $-10\text{ }^{\circ}\text{C}$  shows considerable differences. The rate capacities of

the LIC cell dramatically decay with an increase in current densities. The discharge capacities drop to less than  $38\text{ mA h g}^{-1}$  when the current density increases to  $0.6\text{ C}$ . In contrast, the CNTs cell demonstrates the highest rate capacities at each current density. The discharge capacities of over  $77\text{ mA h g}^{-1}$  are achieved at  $0.6\text{ C}$ . When the current density returns to  $0.1\text{ C}$ , all three cells demonstrate similar cycling stability after 50 cycles with a capacity retention of 96.6% in LIC cell, 95.5% in PEDOT cell, and 95.2% in CNTs cell. The repeatable electrochemical performance is shown in Figure S18 (Supporting Information), proving the reliability of our experiments. The EIS plots before and after battery testing at  $-10\text{ }^{\circ}\text{C}$  are shown in Figures S19 and S20 (Supporting Information). The lowest resistance in CNTs cell after cycling suggests CNTs in the cathode layer did not deteriorate the interfacial stability with LIC SSE, while is beneficial towards the charge transfer. Furthermore, the effect of varying the amount of additives in the cathode layer is investigated

in this study, as shown in Figure S21 (Supporting Information). The results indicate that 1 wt.% CNTs in cathode layer show the best performance. The long cycling stability of the CNTs cell at 0.4 C and  $-10\text{ }^{\circ}\text{C}$  is also demonstrated in Figure 4g. An initial discharge capacity of  $100.4\text{ mA h g}^{-1}$  is achieved with excellent capacity retentions of 99.3% after 100 cycles, 92.1% after 200 cycles, and 89.2% after 300 cycles, respectively. The performance at  $-30\text{ }^{\circ}\text{C}$  is shown in Figure S22 (Supporting Information). The initial capacities of LIC cell and CNTs cell at 0.05 C are 69.2 and  $72.1\text{ mAh g}^{-1}$ , respectively. Interestingly, when the current density increases to 0.1 C, the capacity of the LIC cell drops to zero. In contrast, the CNTs cell still exhibits a capacity of  $40.8\text{ mA h g}^{-1}$  with stable cycling performance. The capacity retention of 98.0% is achieved after 150 cycles. When compared to the low-temperature performance of other SSBs, the performance demonstrated in this work is undoubtedly competitive (Figure 2h; Figure S23 and Table S1, Supporting Information).

The improved rate capability and the stable long-term cycling performance of CNTs cell at  $-10\text{ }^{\circ}\text{C}$  suggest that adding the conductive additives in the cathode layer not only enhances the charge transfer kinetics but also promotes structural and interfacial stability between LIC SSE and LCO cathode. To verify this conclusion, X-ray absorption spectroscopy (XAS) characterizations are first performed to inspect the cycled cathode layer. Figure 5a displays the In K-edge XANES spectra of LIC cell, PEDOT cell, and CNTs cell, respectively. Compared to the In K-edge spectrum of the pristine LIC, there is no detectable whiteline peak shift in the cycled cells. Meanwhile, the highly consistent peak shape and position are shown in the

first derivative spectra (Figure 5b), suggesting a stable valence state and chemical environment of LIC during the cycling. Furthermore, extended X-ray absorption fine structure (EXAFS) spectra of In K-edge obtained by Fourier transform are shown in Figure 5c. The peak at 1.99 Å corresponds to the In–Cl bond.<sup>[16]</sup> The unchanged bond distance and intensity after cycling suggest a stable local structure of LIC after cycling at  $-10\text{ }^{\circ}\text{C}$ . Figure 5d–f shows the XAS spectra of Co K-edge. Similar to the In K-edge spectra, Co K-edge spectra remain the same in all cycled cells, implying excellent structural stability of LCO at  $-10\text{ }^{\circ}\text{C}$ . In addition, the structural stability of LIC in the electrolyte layer is also critical for the performance of SSBs. Therefore, XRD and SEM characterizations are conducted for the cycled LIC in electrolyte layer (Figures S24 and S25, Supporting Information). Both the crystalline structure and morphology of LIC keep the same compared to the pristine LIC, indicating the high stability of LIC in electrolyte layer.

In addition to the structural stability, the interfacial stability in the cathode layer at the low-temperature cycling is further investigated by XPS. The collected In 3d and Cl 2p XPS spectra of the cycled LIC cell, PEDOT cell, and CNTs cell are presented in Figure 6a,b. Compared to the In 3d and Cl 2p XPS spectra of the pristine LIC (Figure S5, Supporting Information), no obvious change is observed in both the In and Cl chemistry in all three cycled cells. This result indicates that LIC SSE is electrochemically stable at  $-10\text{ }^{\circ}\text{C}$ . More importantly, adding the conductive additives in the cathode layer does not induce the decomposition of LIC at low temperatures. Benefitting from the stable interface between LIC and conductive additives,

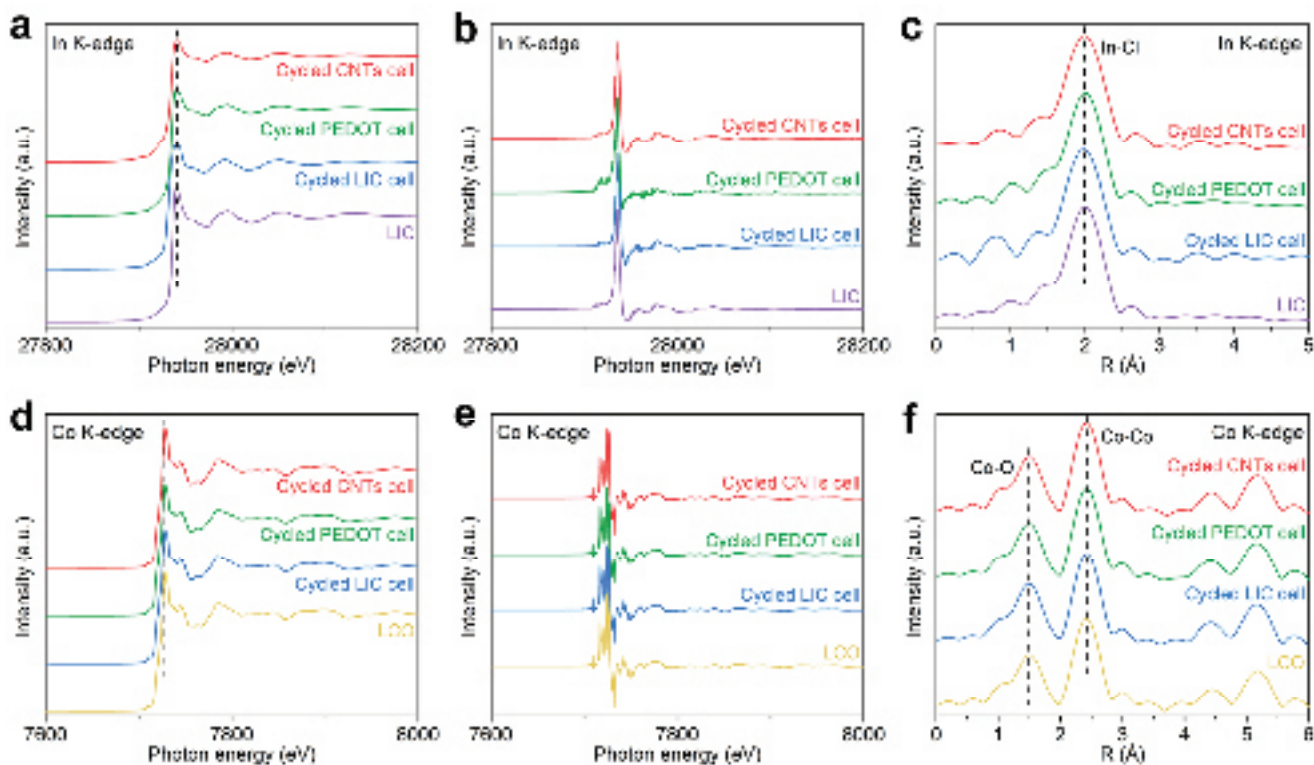


**Figure 5.** Understanding the structural stability of electrode materials after cycling at  $-10\text{ }^{\circ}\text{C}$ . a–c) In K-edge XAS spectra of LIC and d–f) Co K-edge XAS spectra of LIC. a, d) XANES spectra, b, e) the corresponding first derivative spectra, and c, f) Fourier transformed R space EXAFS spectra.

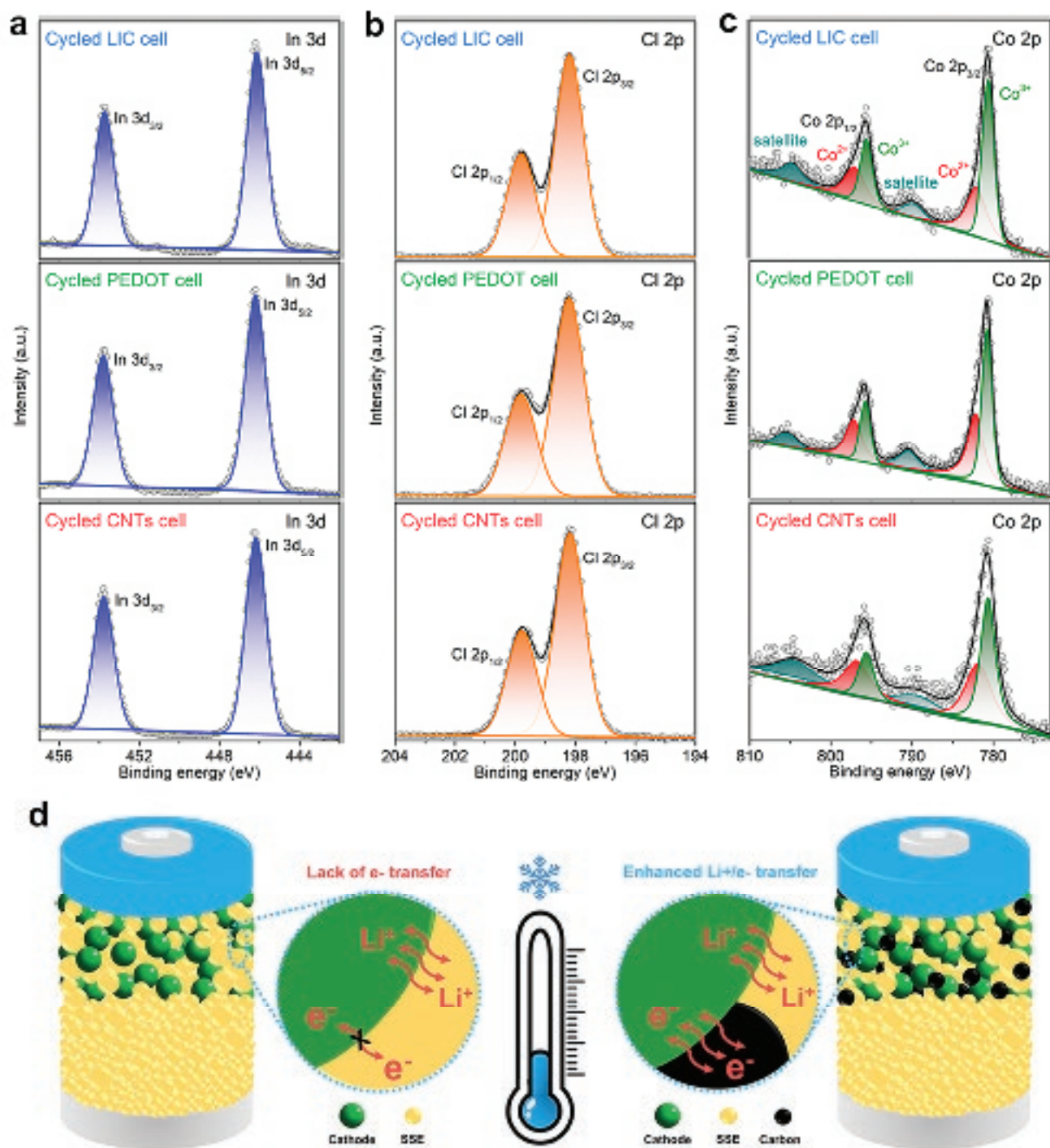


**Figure 6.** Understanding the interfacial stability of composite cathode after cycling at  $-10\text{ }^{\circ}\text{C}$ . a) In 3d, b) Cl 2p, and c) Co 2p XPS spectra of the cycled cells; d) schematic illustration of  $\text{Li}^+$  and electron transfer in composite cathode at low temperatures.

there is also no chemical valence change of Co in all three LCO cathodes after cycling, as shown in Figure 6c and Figure S26 (Supporting Information). Combining both the XAS and XPS results, it can be concluded that the SSBs with conductive additives in cathode layer show excellent structural and interfacial stability at low temperatures. More importantly, increasing the

electronic conductivity at low temperatures is remarkably beneficial toward the charge transfer kinetics at the cathode/SSE/additive three-phase interface (Figure 6d). Unlike room temperature, in which the high ionic conductivity of SSE is enough to provide charge transfer kinetics in cathode layer, halide SSBs face challenge of significantly reduced ionic conductivity

at low temperatures. As a result, charge transfer is struggled in cathode layer, leading to severe polarization. Increasing the electronic conductivity at the cathode/SSE/additive three-phase interface counteracts the negative effect of reduced ionic conductivity, which is critical for the performance of low-temperature halide SSBs.

### 3. Conclusion

In summary, the impact of electronic conductivity in the cathode layer of low-temperature halide-based SSBs is comprehensively investigated by DFT calculations, electrochemical analysis, as well as XPS and XAS characterizations. By designing additives, PEDOT, and CNTs, to manipulate the electronic conductivity in cathode layer, the electrochemical stability of halide SSE is deeply understood at different ambient temperatures. At room temperature, the by-products of LIC SSE are detected, although the degree of decomposition is much lower than that of sulfide SSEs. In contrast, LIC exhibits excellent electrochemical stability with CNTs at both  $-10\text{ }^{\circ}\text{C}$  and  $-30\text{ }^{\circ}\text{C}$ . The electrochemical analysis results indicate that the charge transfer kinetics is significantly improved at low temperatures by adding CNTs in the cathode layer, resulting in enhanced rate capability. A discharge capacity of  $77.6\text{ mAh g}^{-1}$  is achieved under  $0.6\text{ C}$  at  $-10\text{ }^{\circ}\text{C}$ . In addition, the SSB with CNTs shows promising long-term cycling stability at  $-10\text{ }^{\circ}\text{C}$  with a capacity retention of  $89.2\%$  after 300 cycles at  $0.4\text{ C}$ . The results from XAS and XPS characterizations demonstrate excellent structural and interfacial stability of LIC SSE and LCO cathode at low temperatures even after adding high conductive additives in cathode layer. Hence, electronic conductivity in the cathode layer is critical for the performance of halide-based SSBs at low temperatures, which can also improve the performance at room temperature after controlling the conductive additives at a moderate level. Compared to the strategy of using one certain additive and turning the electronic conductivity by different amounts, application of different additives with different electronic conductivities provides a wider choice for different SSB systems. This work opens insights into the low-temperature SSBs and provides valuable guidance for the design of high-performance all-climate SSBs in the future.

### 4. Experimental Section

**DFT Calculation:** All calculations were carried out within the DFT framework as implemented in Vienna Ab Initio Simulation Package (VASP). The projector augmented-wave pseudopotentials were used to describe the interaction between ions and electrons, and the exchange-correlation effects were treated using the Perdew-Burke-Ernzerhof (PBE) functional under the generalized gradient approximation (GGA).<sup>[17]</sup> Herein, the electronic configurations for the PAW potentials were  $1s^2 2s^1$  for Li,  $3s^2 3p^5$  for Cl,  $5s^2 5p^1$  for In,  $2s^2 2p^2$  for C,  $3s^2 3p^4$  for S,  $2s^2 2p^4$  for O, and  $1s^1 2s^0$  for H. The possible structure of  $\text{Li}_3\text{InCl}_6$  (LIC) was generated employing the Supercell code, due to the partial occupation in the unit cell of LIC. The most stable of LIC with lowest energy was chosen in the subsequent calculations. The model of poly(3,4-ethylenedioxythiophene) (PEDOT) contained the simulated cell of 52 atoms. The multi-wall carbon nanotubes (CNTs) were adopted for calculation, where the inner diameter is  $6.84\text{ \AA}$  and outer diameter is  $13.54\text{ \AA}$ . It is noted that there

are two repeated units in CNTs and the total number of carbon atoms is 250. The VESTA package was used to visualize the various bulk, surface, and interface structures.<sup>[18]</sup> The structure of LIC, PEDOT, and CNTs was optimized using kinetic energy cutoffs of  $600\text{ eV}$ , where the  $k$ -points were different, i.e.,  $4 \times 2 \times 4$  for LIC,  $2 \times 4 \times 4$  for PEDOT, and  $\Gamma$ -point for CNTs. All the atoms of structures were optimized until the total energies converged to below  $10^{-5}\text{ eV}$  and the forces acting on atoms were less than  $10^{-2}\text{ eV \AA}^{-1}$ . The density of states for LIC, PEDOT, and CNTs was calculated to determine their corresponding band gap. The electronic transport coefficients were calculated by employing the BoltzTrap code, and especially the electronic conductivity at  $298.15$  and  $263.15\text{ K}$  was calculated. After relaxing the structures of LIC, CNTs, and  $\text{LiCoO}_2$  (LCO), self-consistent calculations were performed to obtain their electrostatic potentials.

**Preparation of Solid-State Electrolytes and Pedot:** For the preparation of solid-state electrolytes (SSEs), LIC was synthesized by a water removal route.  $\text{LiCl}$  and  $\text{InCl}_3$  were dissolved in deionized water with the stoichiometric molar ratio. The solution was dried under a vacuum at both  $100$  and  $200\text{ }^{\circ}\text{C}$ .  $\text{Li}_6\text{PS}_5\text{Cl}$  (LPSCl) was synthesized following the mechanical milling and annealing process.  $\text{Li}_2\text{S}$ ,  $\text{P}_2\text{S}_5$ , and  $\text{LiCl}$  were mixed with the stoichiometric molar ratio and milled at  $550\text{ rpm}$ . After that, the mixture was sealed in a quartz tube and annealed at  $550\text{ }^{\circ}\text{C}$  for  $5\text{ h}$ . PEDOT was fabricated by molecular layer deposition (MLD), in which molybdenum chloride ( $\text{MoCl}_5$ ) and 3,4-ethylenedioxythiophene (EDOT) were used as the precursors. The source temperatures for both  $\text{MoCl}_5$  and EDOT were  $80\text{ }^{\circ}\text{C}$ . The deposition temperature for PEDOT was  $150\text{ }^{\circ}\text{C}$ . During one MLD cycle,  $\text{MoCl}_5$  and EDOT were alternatively introduced into the reaction chamber with a pulse time of  $5\text{ s}$ , and the pulsing of each precursor was separated by a  $60\text{ s}$  purge with  $\text{N}_2$ .

**Assembly of the Solid-State Batteries and Electrochemical Testing:** All of the processes for the cell fabrication were conducted in the Ar filled glovebox. 1) Ionic conductivity: LIC powders were first pressed to form the pellet with a pressure of  $3\text{ tons}$ . The formed pellet was attached with stainless steel rods electrodes. There was no additional stack pressure during the test. The electrochemical impedance spectroscopy (EIS) was conducted at variable temperatures by using versatile multichannel potentiostat 3/Z (VMP3) at frequencies from  $7\text{ MHz}$  to  $1\text{ Hz}$ . 2) Electronic conductivity: Three samples were used for testing, including LIC, mixed LIC/PEDOT, and mixed LIC/CNTs. The electrode progress was same as the cell for ionic conductivity test. The stainless steel was used as the ion-blocking electrodes. Direct current (DC) polarization was conducted for the test of electronic conductivity with the externally applied voltages ranging from  $0.1\text{--}0.5\text{ V}$  with  $1\text{ h}$  for each voltage. 3) Electrochemical stability: LPSCl was used as an interlayer to avoid the contact between LIC and In-Li anode. The cathode layer was prepared in the same method as the cells for the test of electronic conductivity: LIC, mixed LIC/PEDOT, and mixed LIC/CNTs were adopted. The cyclic voltammetry (CV) measurements were scanned at  $0.05\text{ mV s}^{-1}$  from  $2.1\text{--}3.6\text{ V}$  (vs  $\text{Li}^+/\text{Li-In}$ ) for two cycles. Before and after CV tests, EIS measurements were performed with frequencies from  $7\text{ MHz}$  to  $1\text{ Hz}$ . 4) Electrochemical performance: In the cathode layer, the commercial  $\text{LiCoO}_2$  (LCO) cathode and LIC were mixed to form the LIC cell. By adding PEDOT or CNTs in the mixed LCO/LIC, the PEDOT cell and CNTs cell was fabricated as well. First,  $60\text{ mg}$  LIC and  $30\text{ mg}$  LPSCl were pressed at  $2\text{ tons}$  to form an electrolyte layer with  $10\text{ mm}$  diameter.  $10\text{ mg}$  composite cathode (LCO/LIC/additives) with the weight ratio of  $70:30:0.5$ ,  $70:30:1$ ,  $70:30:5$ , or  $70:30:10$  was then pressed on the surface of LIC at  $3\text{ tons}$ . Finally, In-Li anode was put onto the surface of LPSCl with  $0.5\text{ tons}$ . The areal loading of composite cathode is  $12.74\text{ mg cm}^{-2}$ . The galvanostatic charge-discharge characteristics were tested in the range of  $2.1\text{--}3.6\text{ V}$  versus  $\text{Li}^+/\text{Li-In}$ , corresponding to  $2.7\text{--}4.2\text{ V}$  versus  $\text{Li}^+/\text{Li}$  by using a multichannel battery tester (LAND CT-2001A, Wuhan Rambo Testing Equipment Co., Ltd., China). For galvanostatic intermittent titration technique (GITT) measurements, the cells were charged and discharged with  $0.05\text{ C}$  for  $20\text{ min}$  and rest for  $2\text{ h}$ .

**Characterizations:** The morphology and microstructure of the as-prepared composite cathodes and the cycled SSEs were characterized using field emission scanning electron microscopy (FE-SEM, Hitachi

S4800) equipped with an energy dispersive spectrometer (EDS). X-ray powder diffraction (XRD) measurements for the crystalline structure of as-prepared samples were conducted on a Bruker D8 Advance Diffractometer (Cu-K $\alpha$  source, 40 kV, 40 mA). X-ray photoelectron spectroscopy (XPS) testing was measured with a monochromatic Al K $\alpha$  source (1486.6 eV) in a Kratos AXIS Nova Spectrometer. The Ar-filled glovebox was connected with the XPS machine to avoid exposure to air. Synchrotron X-ray studies were carried out at the Canadian Light Source (CLS). X-ray absorption spectroscopy (XAS) data were collected at Hard X-ray Micro Analysis (HXMA) beamline. In K-edge spectra were collected in fluorescence mode using Si(220) crystals, while Co K-edge spectra were also collected in fluorescence mode but using Si(111) crystals. To avoid air exposure, the samples were firstly covered with Kapton tape in glovebox under Ar and then transferred to HXMA for further measurements.

## Supporting Information

Supporting Information is available from the Wiley Online Library or from the author.

## Acknowledgements

This work was supported by the Natural Sciences and Engineering Research Council of Canada (NSERC), Canada Research Chair Program (CRC), Canada Foundation for Innovation (CFI), Ontario Research Fund (ORF), University of Western Ontario, Canadian Light Source, and the University of Toronto. Sixu Deng acknowledges support of a Canada Graduate Scholarships-Doctoral. Chandra Veer Singh acknowledges support from Compute Canada that enabled DFT simulations.

## Conflict of Interest

The authors declare no conflict of interest.

## Data Availability Statement

Research data are not shared.

## Keywords

additives, electronic conductivity, halide electrolytes, low temperature, solid-state batteries

Received: May 16, 2022

Revised: July 6, 2022

Published online:

[1] a) S. Randau, D. A. Weber, O. Kötz, R. Koerver, P. Braun, A. Weber, E. Ivers-Tiffée, T. Adermann, J. Kulisch, W. G. Zeier, *Nat. Energy*

- 2020, 5, 259; b) C. Yang, Q. Wu, W. Xie, X. Zhang, A. Brozena, J. Zheng, M. N. Garaga, B. H. Ko, Y. Mao, S. He, Y. Gao, P. Wang, M. Tyagi, F. Jiao, R. Briber, P. Albertus, C. Wang, S. Greenbaum, Y.-Y. Hu, A. Isogai, M. Winter, K. Xu, Y. Qi, L. Hu, *Nat.* 2021, 598, 590.
- [2] a) D. H. S. Tan, Y.-T. Chen, H. Yang, W. Bao, B. Sreenarayanan, J.-M. Doux, W. Li, B. Lu, S.-Y. Ham, B. Sayahpour, J. Scharf, E. A. Wu, G. Deysheer, H. E. Han, H. J. Hah, H. Jeong, J. B. Lee, Z. Chen, Y. S. Meng, *Sci.* 2021, 373, 1494; b) T. Famprikis, P. Canepa, J. A. Dawson, M. S. Islam, C. Masquelier, *Nat. Mater.* 2019, 18, 1278; c) L. Ye, X. Li, *Nat.* 2021, 593, 218.
- [3] a) L. Zhou, T.-T. Zuo, C. Y. Kwok, S. Y. Kim, A. Assoud, Q. Zhang, J. Janek, L. F. Nazar, *Nat. Energy* 2022, 1, 83; b) J. Liang, X. Li, K. R. Adair, X. Sun, *Acc. Chem. Res.* 2021, 54, 1023.
- [4] a) W. Li, J. Liang, M. Li, K. R. Adair, X. Li, Y. Hu, Q. Xiao, R. Feng, R. Li, L. Zhang, S. Lu, H. Huang, S. Zhao, T.-K. Sham, X. Sun, *Chem. Mater.* 2020, 32, 7019; b) C. Wang, J. Liang, J. Luo, J. Liu, X. Li, F. Zhao, R. Li, H. Huang, S. Zhao, L. Zhang, J. Wang, X. Sun, *Sci. Adv.* 2021, 7, 1896.
- [5] L. M. Riegger, R. Schlem, J. Sann, W. G. Zeier, J. Janek, *Angew. Chem. Int. Ed.* 2021, 60, 6718.
- [6] a) J. Li, S. Li, Y. Zhang, Y. Yang, S. Russi, G. Qian, L. Mu, S. J. Lee, Z. Yang, J. S. Lee, *Adv. Energy Mater.* 2021, 11, 2102122; b) M.-T. F. Rodrigues, G. Babu, H. Gullapalli, K. Kalaga, F. N. Sayed, K. Kato, J. Joyner, P. M. Ajayan, *Nat. Energy* 2017, 2, 17108.
- [7] S. Choi, M. Jeon, B.-K. Kim, B.-I. Sang, H. Kim, *Chem. Comm.* 2018, 54, 14116.
- [8] a) S. Xu, Z. Sun, C. Sun, F. Li, K. Chen, Z. Zhang, G. Hou, H.-M. Cheng, F. Li, *Adv. Funct. Mater.* 2020, 30, 2007172; b) F. Lv, K. Liu, Z. Wang, J. Zhu, Y. Zhao, S. Yuan, *J. Colloid Interface Sci.* 2021, 596, 257.
- [9] a) L. Peng, S. Chen, C. Yu, C. Liao, M. Sun, H.-L. Wang, L. Zhang, S. Cheng, J. Xie, *J. Power Sources* 2022, 520, 230890; b) L. Peng, H. Ren, J. Zhang, S. Chen, C. Yu, X. Miao, Z. Zhang, Z. He, M. Yu, L. Zhang, *Energy Stor. Mater.* 2021, 43, 53.
- [10] F. Zhu, H. Bao, X. Wu, Y. Tao, C. Qin, Z. Su, Z. Kang, *ACS Appl. Mater. Interfaces* 2019, 11, 43206.
- [11] S. Randau, F. Walther, A. Neumann, Y. Schneider, R. S. Negi, B. Mogwitz, J. Sann, K. Becker-Steinberger, T. Danner, S. Hein, *Chem. Mater.* 2021, 33, 1380.
- [12] L. Peng, C. Yu, Z. Zhang, H. Ren, J. Zhang, Z. He, M. Yu, L. Zhang, S. Cheng, J. Xie, *Chem. Eng. J.* 2022, 430, 132896.
- [13] C. Köhler, T. Watermann, A. Knorr, E. Malic, *Phys. Rev. B* 2011, 84, 153407.
- [14] a) D. H. Tan, E. A. Wu, H. Nguyen, Z. Chen, M. A. Marple, J.-M. Doux, X. Wang, H. Yang, A. Banerjee, Y. S. Meng, *ACS Energy Lett.* 2019, 4, 2418; b) J. Liang, X. Li, S. Wang, K. R. Adair, W. Li, Y. Zhao, C. Wang, Y. Hu, L. Zhang, S. Zhao, S. Lu, H. Huang, R. Li, Y. Mo, X. Sun, *J. Am. Chem. Soc.* 2020, 142, 7012.
- [15] S. Deng, Y. Sun, X. Li, Z. Ren, J. Liang, K. Doyle-Davis, J. Liang, W. Li, M. Norouzi Banis, Q. Sun, R. Li, Y. Hu, H. Huang, L. Zhang, S. Lu, J. Luo, X. Sun, *ACS Energy Lett.* 2020, 5, 1243.
- [16] X. Li, J. Liang, N. Chen, J. Luo, K. R. Adair, C. Wang, M. N. Banis, T. K. Sham, L. Zhang, S. Zhao, *Angew. Chem.* 2019, 131, 16579.
- [17] J. P. Perdew, K. Burke, M. Ernzerhof, *Phys. Rev. Lett.* 1996, 77, 3865.
- [18] K. Momma, F. Izumi, *J. Appl. Crystallogr.* 2008, 41, 653.